

## Article

# The BCC/B2 Morphologies in Al<sub>x</sub>NiCoFeCr High-Entropy Alloys

Yue Ma <sup>1</sup>, Beibei Jiang <sup>1</sup>, Chunling Li <sup>1</sup>, Qing Wang <sup>1,\*</sup>, Chuang Dong <sup>1</sup>, Peter K. Liaw <sup>2</sup>, Fen Xu <sup>3</sup> and Lixian Sun <sup>3</sup>

<sup>1</sup> Key Laboratory of Materials Modification by Laser, Ion and Electron Beams (Ministry of Education), School of Materials Science and Engineering, Dalian University of Technology, Dalian 116024, China

<sup>2</sup> Department of Materials Science and Engineering, The University of Tennessee, Knoxville, Tennessee 37996, USA

<sup>3</sup> Guangxi Key Laboratory of Information Materials, Guangxi Collaborative Innovation Center of Structure and Property for New Energy and Materials, School of Material Science and Engineering, Guilin University of Electronic Technology, Guilin 541004, China

\* Correspondence: wangq@dlut.edu.cn; Tel.: +86-411-84708389

**Abstract:** The present work investigates primarily the morphology evolution of the body-centered-cubic (BCC)/B2 phases in Al<sub>x</sub>NiCoFeCr high-entropy alloys (HEAs) with increasing Al content, which has been neglected so far. There exist two types of microscopic morphologies of BCC and B2 phases in this HEA series: one is the weave-like morphology induced by the spinodal decomposition, and the other is the microstructure of a spherical disordered BCC precipitation on the ordered B2 matrix that appears in HEAs with a much higher Al content. The shape of coherent precipitates is found to be closely related to the lattice misfit between BCC and B2 phases, which is sensitive to Al. The mechanical properties, including the compressive yielding strength and microhardness of the Al<sub>x</sub>NiCoFeCr HEAs, are also discussed in light of the concept of the valence electron concentration (VEC).

**Keywords:** high-entropy alloys; Al-Ni-Co-Fe-Cr alloys; microstructure; precipitation morphology; mechanical property

## 1. Introduction

Unlike conventional alloys based on one or two main elements, high-entropy alloys (HEAs) are generally composed of multiple principal elements in equimolar or near-equimolar proportions, also named compositionally-complex alloys (CCAs) [1-6]. This new type of alloys has attracted much attention due to the formation of simple crystalline structures, such as face-centered cubic (FCC)-, body-centered cubic (BCC)-, and close-packed hexagonal (HCP)-solid solutions, as well as their derivatives, instead of complex intermetallic compounds [6-8]. Till now, many HEAs have been reported in diverse systems, e.g., CoCrFeNi-based HEAs [9-14], Al-TMs HEAs (TMs: transition metals) [15-22], and refractory HEAs [23-26]. The special structures render HEAs with the unique performance of excellent mechanical properties and superior corrosion- / oxidation-resistances, as exemplified by the fact that the single FCC CoCrFeMnNi HEA shows a remarkably high fracture toughness that outperforms all conventional alloys at cryogenic temperatures [3, 6, 11].

Typical HEAs were generally formed in Al-containing transition metal (Al-TM) systems, such as Al<sub>x</sub>NiCoFeCr [19-22] and Al<sub>x</sub>NiCoFeCrCu [15-18], in which the crystalline structures change with the increase of Al content. This variation tendency could also be characterized by the valence electron concentration (VEC) that is closely related to the phase stability [27]. For the Al<sub>x</sub>NiCoFeCr HEA series [21], the HEAs with  $x \leq 0.45$  ( $VEC \geq 7.72$ ) exhibit a single FCC phase, HEAs with  $0.45 < x < 0.88$  ( $7.30 < VEC < 7.72$ ), a dual-phase structure of (FCC + BCC), and those with  $x \geq 0.88$  ( $VEC \leq 7.30$ ), a single BCC/B2 phase (B2: an ordered BCC phase with a CsCl-type structure). Consequently, the mechanical properties of this series of HEAs would vary with the crystalline structure. The FCC HEAs possess

good ductility but lower strength, while the BCC/B2 HEAs have higher strength at the expense of ductility, as exemplified by the fact that the equimolar AlNiCoFeCr HEA is very brittle with a nearly zero tensile ductility at room temperature due to a weave-like microstructure caused by spinodal decomposition of BCC and B2 phases [19]. However, that changing the combination of TMs instead of Al could also make the Al<sub>0.7</sub>NiCoFe<sub>2</sub>Cr HEA with a low Al content exhibit a BCC/B2-based structure [28]. More importantly, the unique morphology of the cuboidal B2 phase coherently-embedded into the disordered BCC matrix renders this HEA with both a higher tensile strength ( $\sigma_{UTS}$  = 1223 MPa) and a good ductility of 8 % at room temperature. Although the evolutions of phase structures and mechanical properties with the Al content in the Al<sub>x</sub>CoCrFeNi HEA series have been widely investigated [19-22, 29], the microscopic morphologies of the disordered BCC and its ordered B2 phases have not been studied systematically by far since BCC and B2 phases are always coherent, which is of crucial importance for improving the mechanical property.

Therefore, the present work will aim at the microscopic morphology evolution of the disordered BCC and its ordered B2 phases with increasing the Al content in the Al<sub>x</sub>NiCoFeCr HEA series, in which the coherent morphology of the BCC/B2 phases is closely related to the lattice misfit between them. The compressive mechanical property and Vickers hardness of these HEAs will be measured to show the property variation with the microstructure. The present work will contribute to a better understanding of the B2/BCC coherent morphology in HEAs.

## 2. Experimental

The Al<sub>x</sub>NiCoFeCr serial alloy ingots were synthesized by arc-melting the raw metal materials under argon atmosphere, in which the purities of raw elemental metals are 99.99 % for Al, Co, Fe, Ni, and 99.9 % for Cr, respectively. These ingots with a weight of about 15 g were re-melted at least four times to ensure chemical homogeneity, and then copper-mold suction-cast into cylindrical rods with a diameter of 6 mm. The mass loss during the preparation process is less than 0.1 %.

The crystalline structures of these suction-cast HEAs were analyzed by a Bruker D8 X-ray diffractometer (XRD) with the Cu K $\alpha$  radiation ( $\lambda$  = 0.15406 nm). The morphologies of HEAs were observed by both Olympus optical microscopy (OM) and Zeiss Supra55 scanning-electron microscopy (SEM) with an etching solution of 5g FeCl<sub>3</sub>·6H<sub>2</sub>O + 25ml HCl + 25ml C<sub>2</sub>H<sub>5</sub>OH. The further detailed microstructures of HEAs were characterized by the Philips Tecnai G2 transmission-electron microscopy (TEM) with a selected-area electron diffraction (SAED) analysis, in which the TEM samples were prepared by twin-jet electro-polishing in a solution of 10 % HClO<sub>4</sub> + 90 % C<sub>2</sub>H<sub>5</sub>OH (volume fraction) at about - 30 °C. The elemental distributions and compositional analysis were measured by the SHIMADZU electron-probe microanalysis (EPMA). The uniaxial compressive test was performed on an 810 Material Test System (MTS) with a strain rate of  $2 \times 10^{-4}$  /s at room temperature, in which a strain gage was used for the strain measurement. Two specimens for each alloy were tested with a size of  $\phi 3 \times 6$  mm, which were machined from the  $\phi 6$  mm alloys rods. Microhardness of HEAs was measured with a HVS-1000 Vickers hardness tester under a load of 500 g for 20 s, in which at least 15 indents were tested to obtain an average value.

## 3. Experimental results

### 3.1. Microstructural characterization

Alloy compositions in atomic percent (at. %) of this Al<sub>x</sub>NiCoFeCr HEA series are listed in Table 1, and all alloys are marked with Al<sub>x</sub> hereafter. The XRD results of these suction-cast alloys are shown in Figure 1, from which the Al<sub>0.41</sub> alloy (S1) with a lower Al content of 9.38 at. % exhibits a single FCC solid solution structure, and the BCC and its ordered B2 phases will appear with increasing the Al content. There exist obvious diffraction peaks of the BCC/B2 phases in the Al<sub>0.57</sub> alloy (S2, 12.5 at. % Al) although its matrix is still FCC. Then, the BCC and B2 phases are dominant in high-Al HEAs, as exemplified by the Al<sub>0.74</sub> alloy (S3, 15.63 at. % Al), and the FCC phase will disappear in the alloys with the Al content larger than 18 at. %, as seen in the XRD patterns of Al<sub>0.92</sub> (S4), Al<sub>1.12</sub> (S5), and Al<sub>1.33</sub> (S6). This trend will be verified further by the OM observations.

**Table 1.** The alloy compositions, valence electron concentration (VEC), Vickers hardness (HV), compressive mechanical property (yielding strength  $\sigma_y$  and plasticity  $\epsilon$ ), and phase constitution of the  $\text{Al}_x\text{NiCoFeCr}$  HEA series.

No.	Alloy compositions		VEC <sup>1</sup>	HV	$\sigma_y$ (MPa)	$\epsilon$ (%)	Phase constitution
	molar proportion	atomic percent (at. %)					
S1	$\text{Al}_{0.41}\text{NiCoFeCr}$ ( $\text{Al}_{0.41}$ )	$\text{Al}_{9.38}\text{Ni}_{22.66}\text{Co}_{22.66}\text{Fe}_{22.66}$ $\text{Cr}_{22.66}$	7.76	178	255	without fracture	FCC matrix +minor BCC
S2	$\text{Al}_{0.57}\text{NiCoFeCr}$ ( $\text{Al}_{0.57}$ )	$\text{Al}_{12.5}\text{Ni}_{21.88}\text{Co}_{21.88}\text{Fe}_{21.88}$ $\text{Cr}_{21.88}$	7.59	272	607	36	FCC matrix +BCC/B2
S3	$\text{Al}_{0.74}\text{NiCoFeCr}$ ( $\text{Al}_{0.74}$ )	$\text{Al}_{15.63}\text{Ni}_{21.09}\text{Co}_{21.09}\text{Fe}_{21.09}$ $\text{Cr}_{21.09}$	7.43	529	1394	24	BCC/B2 matrix +minor FCC
S4	$\text{Al}_{0.92}\text{NiCoFeCr}$ ( $\text{Al}_{0.92}$ )	$\text{Al}_{18.75}\text{Ni}_{20.31}\text{Co}_{20.31}\text{Fe}_{20.31}$ $\text{Cr}_{20.31}$	7.27	531	-	-	BCC/B2
S5	$\text{Al}_{1.12}\text{NiCoFeCr}$ ( $\text{Al}_{1.12}$ )	$\text{Al}_{21.88}\text{Ni}_{19.53}\text{Co}_{19.53}\text{Fe}_{19.53}$ $\text{Cr}_{19.53}$	7.10	527	1366	17	BCC/B2
S6	$\text{Al}_{1.33}\text{NiCoFeCr}$ ( $\text{Al}_{1.33}$ )	$\text{Al}_{25.00}\text{Ni}_{18.75}\text{Co}_{18.75}\text{Fe}_{18.75}$ $\text{Cr}_{18.75}$	6.94	517	1348	14	BCC/B2

$$^1 \text{VEC} = \sum C_i * (\text{VEC})_i$$

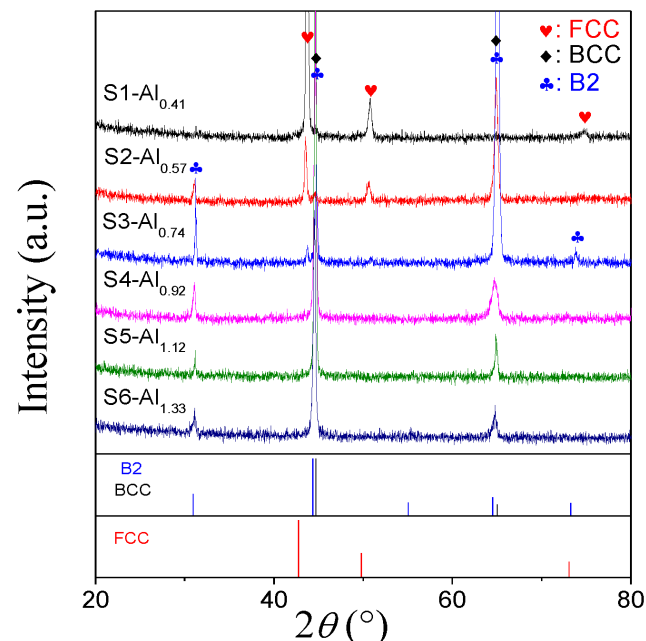


**Figure 1.** XRD patterns of the suction-cast  $\text{Al}_x\text{NiCoFeCr}$  HEAs.

The main matrix of the  $\text{Al}_{0.41}$  alloy (S1) shows bright FCC dendrites, as shown in Figure 2(a), in which a small amount of BCC/B2 phases is distributed in the inter-dendritic regions (dark region) that could not be detected by XRD. The amount of the inter-dendritic BCC/B2 phases increases with Al, as evidenced by the  $\text{Al}_{0.57}$  alloy (S2, Fig. 2(b)). In the  $\text{Al}_{0.74}$  alloy (S3, Fig. 2(c)), the BCC/B2 phases show a microstructure of coarse columnar dendrites, and a minor of FCC phase is in the region of inter-dendrites. With further increasing Al, the flower-like dendrites are distributed in the matrix (Fig. 2(d-f)), which is resulted from the composition segregation.

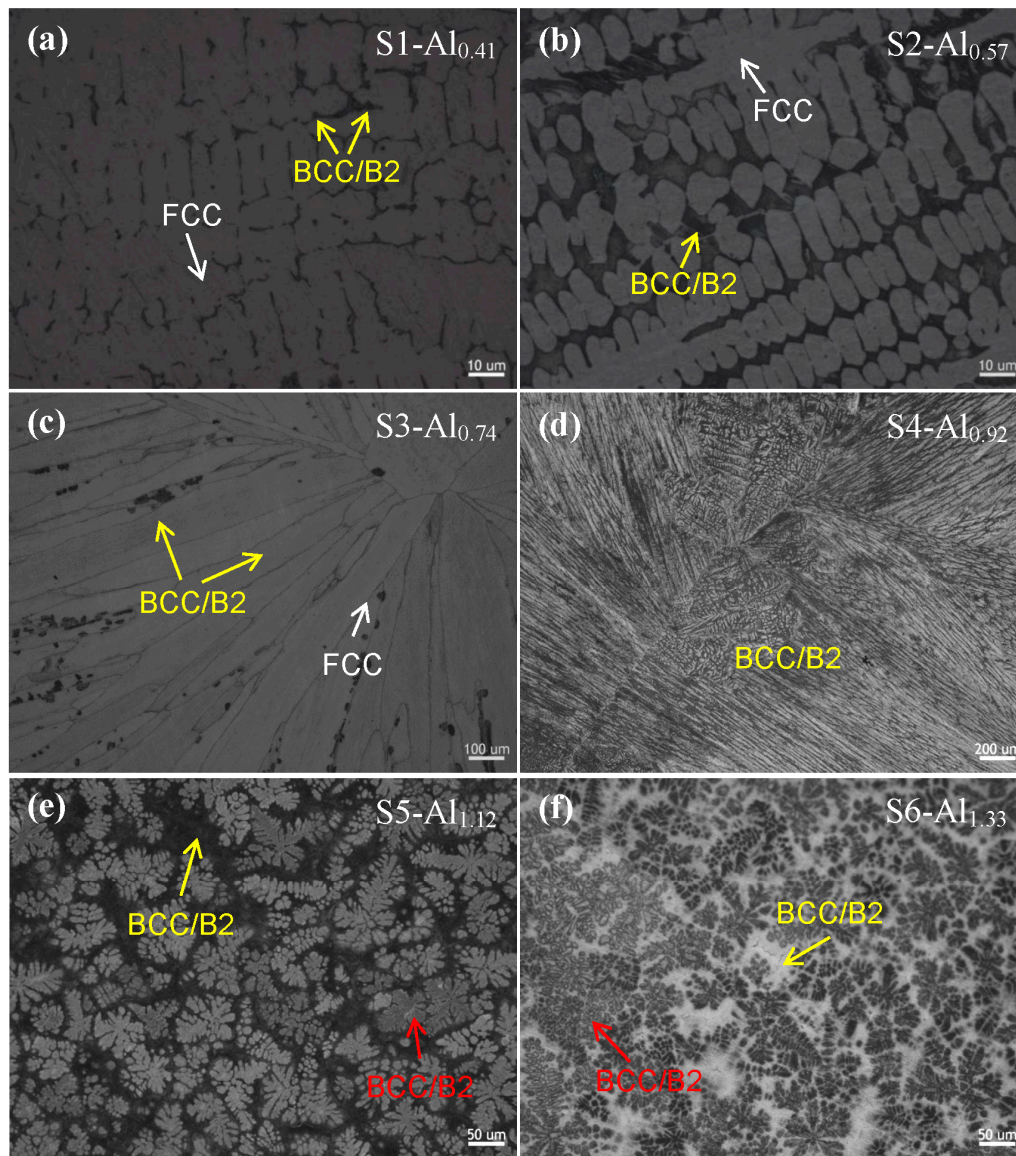


**Figure 2.** Optical microscopy (OM) graphs of the Al<sub>k</sub>NiCoFeCr HEAs. (a): S1-Al<sub>0.41</sub>, (b): S2-Al<sub>0.57</sub>, (c): S3-Al<sub>0.74</sub>, (d): S4-Al<sub>0.92</sub>, (e): S5-Al<sub>1.12</sub>, (f): S6-Al<sub>1.33</sub>.

Figure 3 gives the elemental distributions of the Al<sub>1.12</sub> alloy (S5) measured by EMPA, from which it could be found that much greater amounts of Al and Ni are aggregated in the flower-like dendrites, and the other inter-dendrites contain much greater contents of Fe and Cr. The measured compositions of the flower-like dendrites and the inter-dendrites are Al<sub>26.01</sub>Ni<sub>23.80</sub>Co<sub>20.23</sub>Fe<sub>16.22</sub>Cr<sub>13.74</sub> and Al<sub>17.21</sub>Ni<sub>18.73</sub>Co<sub>19.77</sub>Fe<sub>21.70</sub>Cr<sub>22.59</sub> (at. %), respectively, different obviously from the nominal composition of Al<sub>21.88</sub>Ni<sub>19.53</sub>Co<sub>19.53</sub>Fe<sub>19.53</sub>Cr<sub>19.53</sub> (at. %). In addition, it is noted that both the flower-like dendrites and the inter-dendrites have BCC and B2 structures without any FCC phase, as evidenced by XRD and the following SEM and TEM studies.



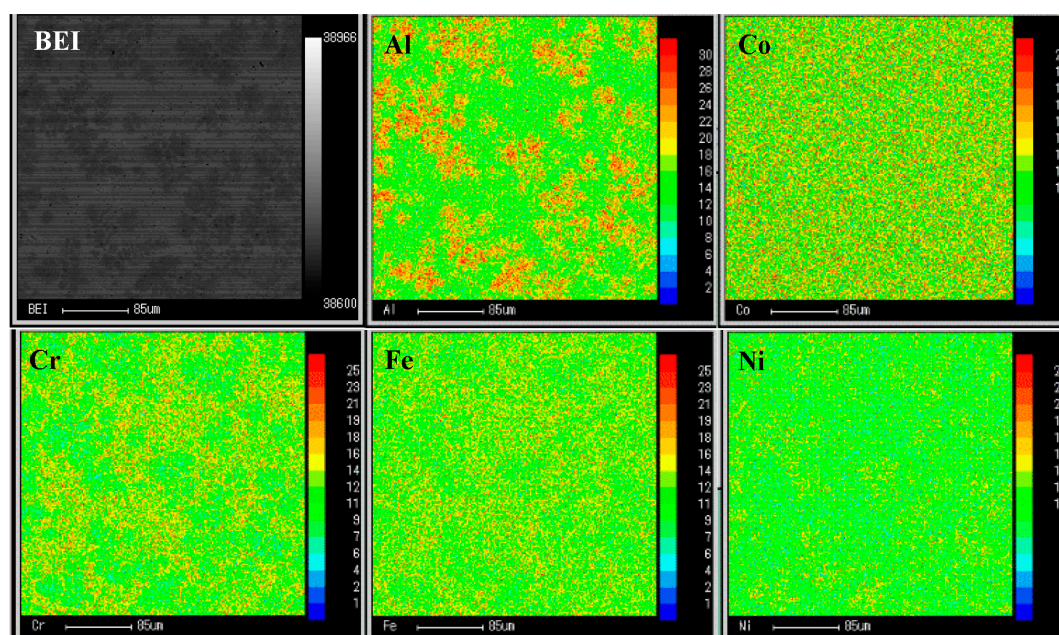


**Figure 3.** Elemental distributions of the S5-Al<sub>1.12</sub> HEA mapped by the electron-probe microanalysis (EPMA).

The specific microscopic morphologies of BCC/B2 phases in this HEA series are revealed by highly-magnified SEM images (Fig. 4), in which the disordered BCC and its ordered B2 phases always exist coherently. Even in the FCC-based HEAs of Al<sub>0.41</sub> (S1, Fig. 4(a)) and Al<sub>0.57</sub> (S2, Fig. 4(b)), the BCC and B2 phases are coherent in the inter-dendrites with a weave-like morphology caused by spinodal decomposition. Such a morphology still exists in the BCC Al<sub>0.74</sub> (S3, Fig. 4(c)) and Al<sub>0.92</sub> alloys (S4, Fig. 4(d)). When two typical BCC/B2 microstructures induced by composition segregation are different obviously, the microscopic morphologies of BCC/B2 phases would be changed. Take the Al<sub>1.12</sub> alloy (S5, Fig. 4(g-i)) for instance. In the flower-like dendrites (dark regions in Fig. 4(g)), it is found that spherical nanoparticles are embedded into the matrix (Fig. 4(i)), while the inter-dendrites (bright region in Fig. 4(g)) still show a weave-like morphology (Fig. 4(h)), similar to those in S1-S4 HEAs.

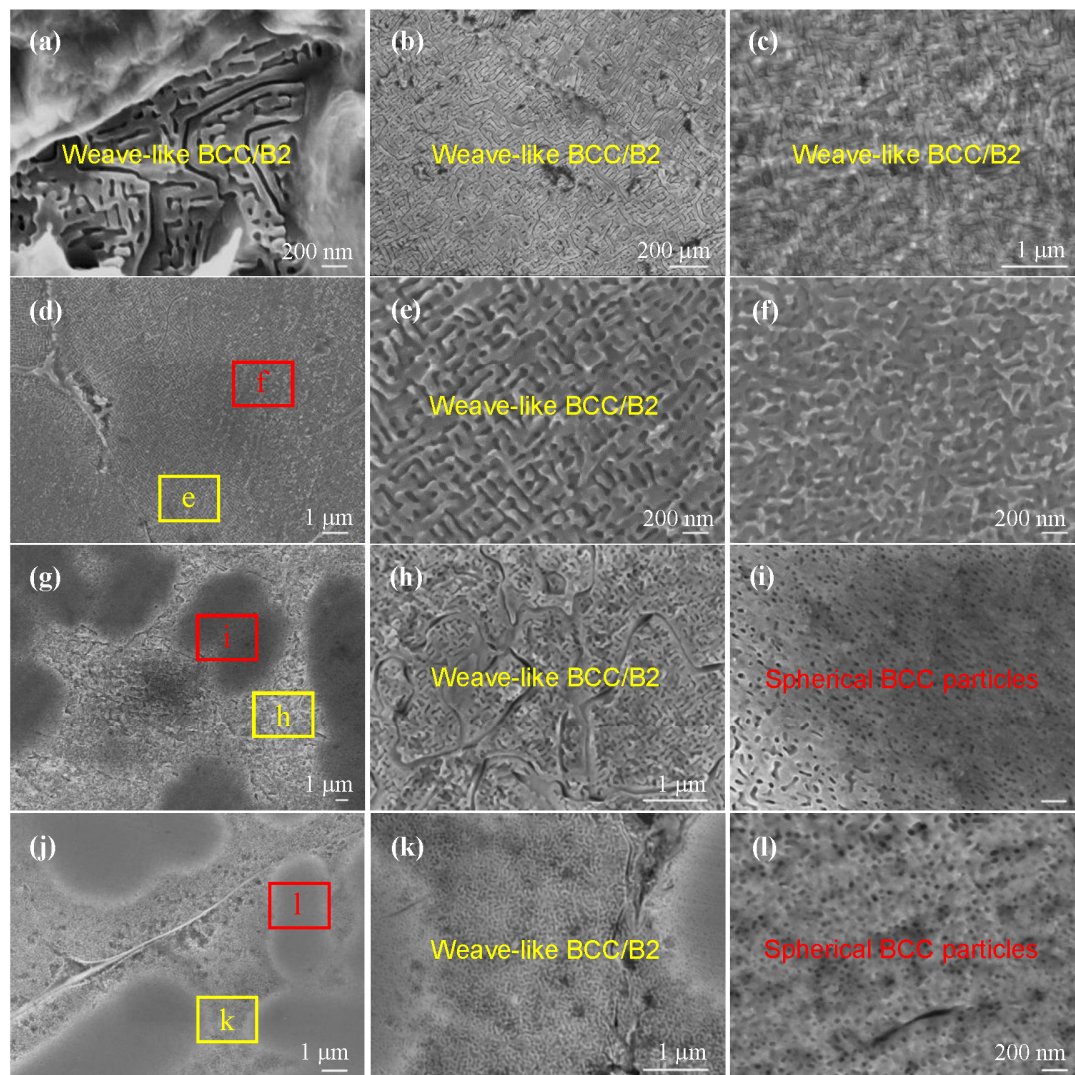


**Figure 4.** SEM morphologies of the  $\text{Al}_x\text{NiCoFeCr}$  HEAs. (a):  $\text{S1-Al}_{0.41}$ , (b):  $\text{S2-Al}_{0.57}$ , (c):  $\text{S3-Al}_{0.74}$ , (d-f):  $\text{S4-Al}_{0.92}$ , (g-i):  $\text{S5-Al}_{1.12}$ , (j-l):  $\text{S6-Al}_{1.33}$ . Besides the weave-like morphology of BCC and B2 phases, there exists another type of microstructures of spherical BCC nanoparticles distributed in the B2 matrix of high-Al HEAs.

With the further TEM results (Fig. 5), the spherical particles with a diameter of about 50 nm are identified as a BCC phase by the dark-field image and SAED pattern (Fig. 5(b)). That is to say, it is the spherical BCC nanoparticles that are coherently precipitated on the ordered B2 matrix in the flower-like dendrites. While the weave-like spinodal decomposition of BCC and B2 phases appears in the inter-dendrites (Fig. 5(a, c)). Similar morphologies of BCC and B2 phases also appear in the  $\text{Al}_{1.33}$  alloy (S6, Fig. 4(j-l)) with spherical particles in the flower-like dendrites and weave-like spinodal morphology in the other part, in which the size of spherical particles is much smaller, being approximately 20 nm (Fig. 5(d)).



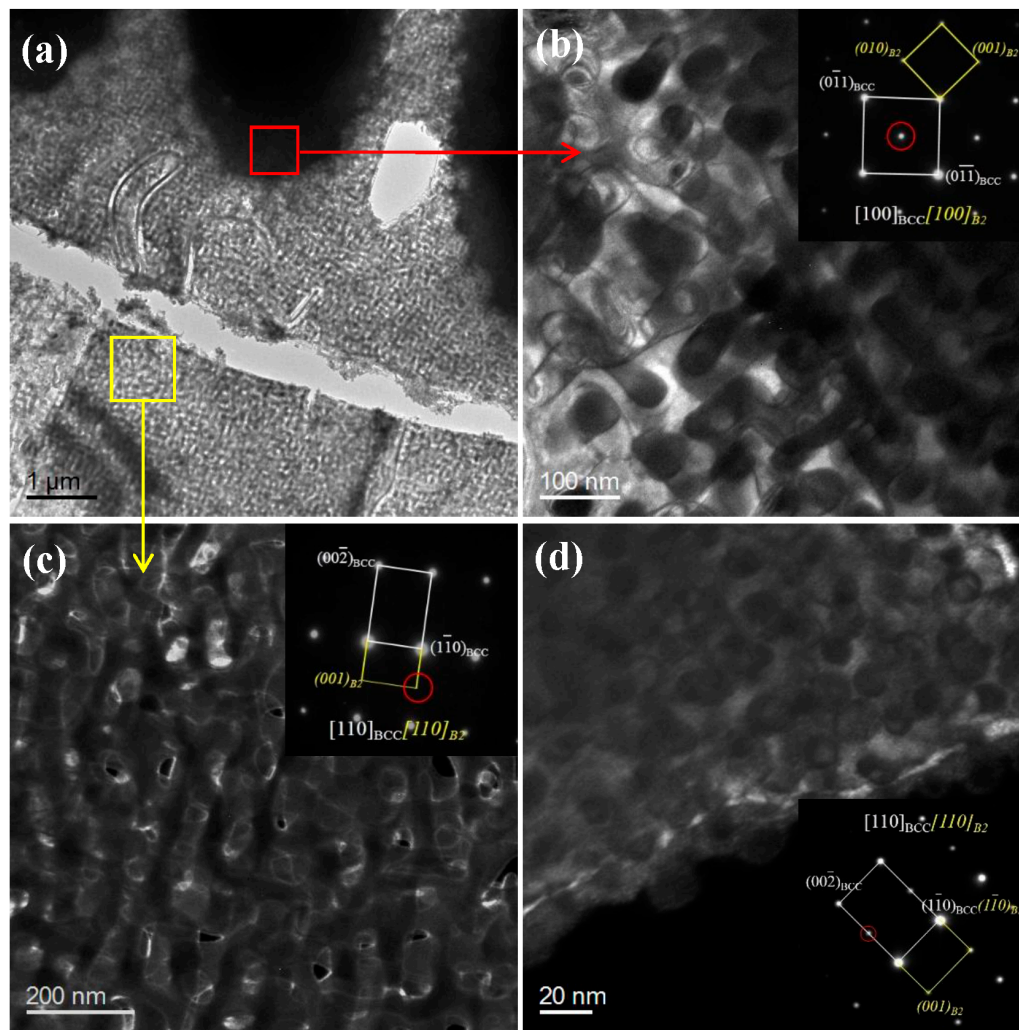


**Figure 5.** TEM images of the S5-Al<sub>1.12</sub> (a-c) and S6-Al<sub>1.33</sub> (d) HEAs. (a) is the bright-field image of S5, (b) and (c) are the magnified dark-field images corresponding to regions in (a) marked with the red and yellow rectangles, respectively, showing two types of morphologies of BCC and B2 phases: a morphology of spherical BCC nanoparticles [the SAED pattern in the inset of (b)] coherently precipitated in the BCC matrix and a weave-like morphology by spinodal decomposition (c). (d) is the dark-field image of S6, also showing spherical BCC nanoprecipitates by the SAED pattern in the inset.

### 3.2. Mechanical properties

Figure 6 shows engineering compressive stress-strain curves of this Al<sub>x</sub>CoCrFeNi HEA series (except the Al<sub>0.92</sub> alloy (S4)), from which the compressive yielding strength  $\sigma_Y$  and plasticity  $\varepsilon$  are measured and listed in Table 1. The FCC-based alloy, S1-Al<sub>0.41</sub>, exhibits a good compressive plasticity but a relatively-lower strength with  $\sigma_Y = 255$  MPa. With the amount of the inter-dendritic BCC/B2 phases increases, the strength is enhanced up to  $\sigma_Y = 607$  MPa (S2-Al<sub>0.57</sub>). When the BCC/B2 phases are dominant in HEAs, the compressive  $\sigma_Y$  could be enhanced drastically, and keeps constant at a high strength level of 1350 ~ 1400 MPa (S3-S6 HEAs). For example, the compressive yielding strength of the Al<sub>0.74</sub> alloy (S3) is  $\sigma_Y = 1394$  MPa, much higher than the FCC-based HEAs, even about 5 times than that of the FCC-based Al<sub>0.41</sub> alloy. In addition, Table 1 also lists the measured Vickers hardness (*HV*) of these HEAs, in which the tendency of *HV* with the crystalline structure is similar to that of the yielding strength.

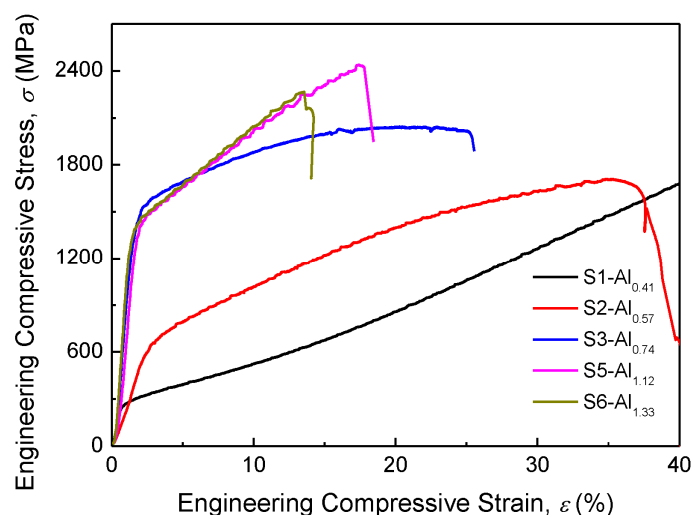


**Figure 6.** Engineering compressive stress-strain curves of the Al<sub>x</sub>NiCoFeCr HEAs.

## 4. Discussion

### 4.1. Microscopic morphologies of BCC/B2 phases in HEAs

It could be found obviously that whenever the FCC-based HEAs with a low Al content or the BCC/B2 HEAs with a high Al content in the Al<sub>x</sub>NiCoFeCr series are present, the ordered B2 phase is always coherent with the disordered BCC phase in the BCC-related regions, as shown in Figures 5 and 6. However, their microscopic morphologies might be different. For instance, in the interdendritic regions of the FCC-based Al<sub>0.41</sub> alloy with a lower Al content of 9.38 at. %, the BCC and B2 phases show a weave-like morphology caused by spinodal decomposition (Fig. 4(a)), which is a typical microstructure in many BCC-based HEAs [20–21]. In the Al<sub>1.12</sub> alloy (S5) with a high Al content of 21.88 at. %, besides this kind of weave-like morphology, the other kind of morphology of spherical BCC nanoparticles coherently embedded into B2 matrix appears in the flower-like dendrites (Fig. 4(i), and Fig. 5(b)). Such a morphology of spherical precipitation of the BCC phase also appears in the Al<sub>1.33</sub> alloy (S6 Fig. 4(l) and Fig. 5(d)). These two kinds of BCC/B2 microstructures are resulted from the composition segregation, which could be also verified by the XRD results that the diffraction peaks of BCC and B2 phases are widened clearly (Fig. 1). Thereof, in the BCC/B2 regions with a very high Al content, the ordered B2 phase becomes the matrix, and the disorder BCC is the precipitated phase with a spherical morphology, which is contrary to the common image that the ordered phase is always precipitated on the disordered BCC matrix [30–35].

It is known that the size and the shape of precipitates are crucial for the mechanical properties of conventional alloys. Especially, the shape of the precipitates is closely related to the lattice misfit,  $\varepsilon$ , between the precipitated phase and the matrix phase [28, 30–37]. Generally speaking, a smaller lattice misfit,  $\varepsilon$ , leads to a spherical shape, and when the misfit becomes larger, it is difficult to control the morphology of the precipitates, and the coherency between them will disappear gradually, resulting in coarse second particles finally. Only a moderate  $\varepsilon$ , neither large nor small, can produce cuboidal coherent precipitates, leading to excellent mechanical properties. Such a case is common in Ni-based superalloys [32–33], in which the cuboidal ordered nanoparticles with a L1<sub>2</sub> structure (Ni<sub>3</sub>Al-type) are coherently embedded into the disordered FCC matrix, exhibiting an incomparable mechanical property at high temperatures. While in sharp contrast, the weave-like spinodal morphology of ordered and disordered coherent phases with a relatively-larger  $\varepsilon$  will deteriorate alloy properties, as exemplified by the brittle AlNiCoFeCr HEA [19].

Take the disordered BCC and ordered B2 phases for instance. The lattice misfit can be calculated with the formula of  $\varepsilon = 2 * (\alpha_{B2} - \alpha_{BCC}) / (\alpha_{B2} + \alpha_{BCC})$ , where  $\alpha_{B2}$  and  $\alpha_{BCC}$  are the lattice constants of B2 and BCC phases, respectively. Here, the lattice constants of BCC and B2 phases in Al<sub>0.57</sub> (S2), Al<sub>0.74</sub> (S3), and Al<sub>0.92</sub> (S4) HEAs were calculated from XRD, and those in Al<sub>1.12</sub> (S5) and Al<sub>1.33</sub> (S6) HEAs were



achieved from TEM. Table 2 lists these lattice constants ( $a_{B2}$  and  $a_{BCC}$ ), lattice misfits  $\varepsilon$ , and their corresponding microscopic morphologies of BCC and B2 phases. It could be concluded that a larger absolute value of  $\varepsilon$  ( $\varepsilon > 0.53$  %) corresponds to a weave-like morphology caused by the spinodal decomposition of BCC and B2 phases. A smaller  $\varepsilon$  ( $\varepsilon < 0.10$  %) can produce another morphology of spherical particles coherently precipitated into the matrix. Only a moderate  $\varepsilon$  can produce cuboidal precipitates, as exemplified by the fact that the cuboidal B2 nanoprecipitates are coherently embedded into the BCC matrix in the BCC  $Al_{0.57}NiCoFe_2Cr$  HEA with a  $\varepsilon = -0.38$  % [28].

**Table 2.** The lattice misfits  $\varepsilon$  and the corresponding morphologies of BCC and B2 phases in the  $Al_xNiCoFeCr$  HEAs, in which the lattice constants ( $a_{B2}$  and  $a_{BCC}$ ) of BCC and B2 phases calculated from both XRD and TEM analysis are also included.

No.	$a_{B2}$ (Å)	$a_{BCC}$ (Å)	$\varepsilon$ <sup>1</sup> (%)	Morphology
S2- $Al_{0.57}$	2.871	2.854	0.59	weave-like spinodal decomposition
S3- $Al_{0.74}$	2.855	2.870	-0.53	weave-like
S4- $Al_{0.92}$	2.878	2.897	-0.69	weave-like
S5- $Al_{1.12}$	2.809	2.831	-0.78	weave-like
	2.855	2.858	-0.11	spherical particles
S6- $Al_{1.33}$	2.908	2.911	-0.10	spherical particles
$Al_{0.7}NiCoFe_2Cr$ [28]	2.851	2.862	-0.38	cuboidal particles

$$^1 \varepsilon = 2 * (a_{B2} - a_{BCC}) / (a_{B2} + a_{BCC})$$

In fact, the weave-like morphology of BCC and B2 phases is common in the Al-containing BCC HEAs, which is due to that Al affects the lattice constants of BCC and B2 strongly, leading to a large lattice misfit  $\varepsilon$ . Moreover, the  $\varepsilon$  could increase with the Al content, as a result of a serious spinodal decomposition. Similar to Al, the elements Ti and Zr also can produce a larger misfit, as exemplified by the fact that the lattice misfit of  $\varepsilon = 2.38$  % between BCC and B2 phases in the refractory  $Al_{0.3}NbTaTi_{1.4}Zr_{1.3}$  BCC HEA is so high that a consequent spinodal decomposition deteriorate the plasticity seriously [23]. Thereof, it is difficult to obtain a moderate lattice misfit of BCC and B2 phases for an expected morphology through tuning Al (Ti, Zr) in BCC-based HEAs since they affect the lattice constants obviously.

#### 4.2. Relationship among $\sigma_Y$ , HV, and structure with VEC of HEAs

It is well known that the phase stability of an alloy is related to multiple factors simultaneously, such as the atom size, electron concentration, and enthalpy of mixing [38-41]. Here the valence electron concentration (VEC) is introduced to characterize the strength evolution of the designed HEAs due to its simplicity. It can be calculated with the formula of  $VEC = \sum C_i * (VEC)_i$ , where  $C_i$  is the atomic percentage and  $(VEC)_i$  is the VEC value for the  $i$  element, being 3 for Al, 6 for Cr, 8 for Fe, 9 for Co, and 10 for Ni, respectively. Figure 7 shows the compressive yielding strength,  $\sigma_Y$ , and Vickers hardness, HV, as a function of VEC of this HEA series, in which the VEC for the characterization of the BCC/B2 region is  $VEC < 7.4$ . The  $\sigma_Y$  and HV of HEAs with a dual-phase of BCC and FCC HEAs would be obviously enhanced with increasing the amount of the BCC/B2 phases. While the  $\sigma_Y$  and HV of the BCC HEAs keep almost constant at a relatively-higher strength level ( $\sigma_Y = 1350 \sim 1400$  MPa,  $HV = 520 \sim 530$ ) at the expense of plasticity with decreasing VEC (Tab. 1). In comparison with the BCC-based  $Al_{0.7}NiCoFe_2Cr$  HEA ( $Al_{12.5}Ni_{17.5}Co_{17.5}Fe_{35.0}Cr_{17.5}$  at. %,  $VEC = 7.55$ ) with cuboidal B2 nanoprecipitates coherent with the BCC matrix [28], exhibiting a compressive strength of  $\sigma_Y = 1166$  MPa ( $HV = 486$ ) and a plasticity of  $\varepsilon = 30.2$  %, the  $Al_{0.74}$  alloy (S2) with the same Al content exhibits a FCC matrix with a relatively-lower strength ( $\sigma_Y = 607$  MPa). While the plasticity of this BCC

Al<sub>x</sub>NiCoFeCr series with high Al contents are decreased obviously although they have a higher strength (Tab. 1 and Fig. 6). Therefore, that changing the combination of transition metals to substitute for the Al could achieve a moderate lattice misfit for the cuboidal morphology of B2 precipitates in the BCC matrix, which renders the HEAs with high strength and good ductility.

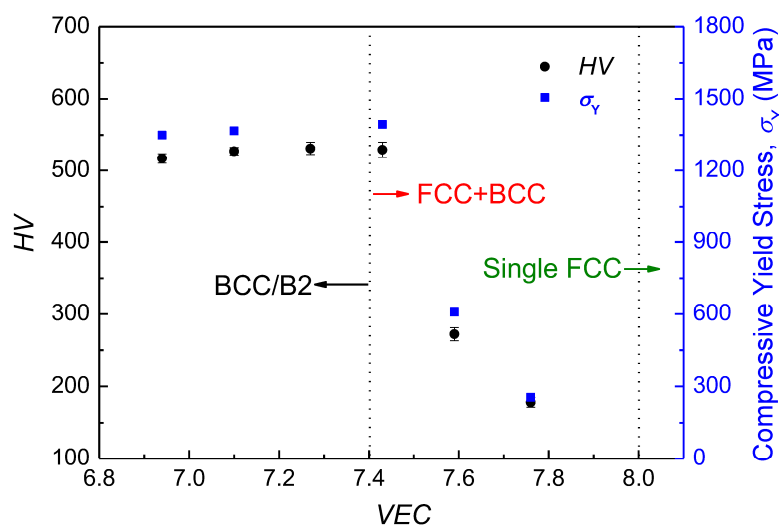


**Figure 7.** The tendencies of compressive yielding stress,  $\sigma_y$ , and microhardness,  $HV$ , with  $VEC$  of the Al<sub>x</sub>NiCoFeCr HEAs.

## 5. Conclusions

The evolutions of microstructures and mechanical properties of the Al<sub>x</sub>NiCoFeCr HEA series have been studied with changing the Al content, in which the microscopic morphologies of disordered BCC and ordered B2 phases are investigated particularly. It is found that the B2 phase is always coherently present with the BCC phase in the BCC-related regions of both FCC-based and BCC HEAs. There are two typical morphologies of BCC/B2 phases in this alloy series, one being the weave-like spinodal morphology and the other the morphology of spherical BCC nanoprecipitates in the B2 matrix. The shapes of coherent precipitates are closely related to the absolute value of the lattice misfit,  $\epsilon$ , between BCC and B2 phases, in which a small  $\epsilon$  ( $\epsilon < 0.10\%$ ) could produce a spherical precipitation and a larger  $\epsilon$  ( $\epsilon > 0.53\%$ ) corresponds to a weave-like spinodal decomposition that is sensitive to Al. The Al<sub>x</sub>NiCoFeCr BCC HEAs possess a higher strength (compressive  $\sigma_y = 1350 \sim 1400$  MPa) at the expense of plasticity. That tuning the combination of transition metals instead of Al is expected to obtain a moderate  $\epsilon$  for cuboidal precipitation, which will lead to prominent mechanical properties.

**Acknowledgments:** This work was supported by the National Natural Science Foundation of China (No. 51171035), the International Science & Technology Cooperation Program of China (No. 2015DFR60370), the Natural Science Foundation of Liaoning Province of China (No. 2015020202), the Foundation of Guangxi Key Laboratory of Information Materials [No. 161002-K], and the Fundamental Research Funds for the Central Universities (No. DUT16ZD212). Prof. P.K. Liaw would like to acknowledge the Department of Energy (DOE), Office of Fossil Energy, National Energy Technology Laboratory (DE-FE-0008855, DE-FE-0024054, and DE-FE-0011194), the U.S. Army Research Office project (W911NF-13-1-0438), the National Science Foundation (DMR-1611180), and the QuesTek Innovations LLC (No. DE-SC0013220).

**Author Contributions:** Qing Wang conceived and designed the experiments; Yue Ma performed the experiments, analyzed the data and wrote the paper; Beibei Jiang and Chunling Li gave assistance about experiments; Chuang Dong and Peter K. Liaw discussed the results and modified the paper; Fen Xu and Lixian Sun contributed reagents/materials.

**Conflicts of Interest:** The authors declare no conflicts of interest.

## References

1. Miracle, D.B.; Senkov, O.N. A critical review of high entropy alloys and related concepts. *Acta Mater.* 2016, 122, 488–511.
2. Senkov, O.N.; Miller, J.D.; Miracle, D.B.; Woodward, C. Accelerated exploration of multi-principal element alloys with solid solution phases. *Nature Comm.* 2015, 6, 7529.
3. Zhang, Y.; Zuo, T.T.; Tang, Z.; Gao, M.C.; Dahmen, K.A.; Liaw, P.K.; Lu, Z.P. Microstructures and properties of high-entropy alloys. *Prog. Mater. Sci.* 2014, 61, 1–93.
4. Ye, Y.F.; Wang, Q.; Lu, J.; Liu, C.T.; Yang, Y. High-entropy alloy: challenges and prospects. *Mater. Today* 2016, 19, 349–362.
5. Yeh, J.W.; Chen, S.K.; Lin, S.J.; Gan, J.Y.; Chin, T.S.; Shun, T.T.; Tsau, C.H.; Chang, S.Y. Nanostructured high-entropy alloys with multiple principal elements: Novel alloy design concepts and outcomes. *Adv. Eng. Mater.* 2004, 6, 299–303.
6. Diao, H.; Xie, X.; Sun, F.; Dahmen, K.A.; Liaw, P.K. Mechanical Properties of High-Entropy Alloys. In *High-Entropy Alloys: Fundamentals and Applications*; Gao, M.C., Yeh, J.W., Liaw, P.K., Zhang, Y., Eds.; Springer International Publishing, CH, 2016; pp. 181–236.
7. Zhang, Y.; Zhou, Y.J.; Lin, J.P.; Chen, G.; Liaw, P.K. Solid-solution phase formation rules for multi-component alloys. *Adv. Eng. Mater.* 2008, 10, 534–538.
8. Youssef, K.M.; Zaddach, A.J.; Niu, C.; Irving, D.L.; Koch, C.C.; A Novel Low-Density, High-Hardness, High-entropy Alloy with Close-packed Single-phase Nanocrystalline Structures. *Mater. Res. Lett.* 2014, 2, 95–99.
9. Schuh, B.; Mendez-Martin, F.; Volker, B.; George, E.P.; Clemens, H.; Pippin, R.; Hohenwarter, A. Mechanical properties, microstructure and thermal stability of a nanocrystalline CoCrFeMnNi high-entropy alloy after severe plastic deformation. *Acta Mater.* 2015, 96, 258–268.
10. Salishchev, G.A.; Tikhonovsky, M.A.; Shaysultanov, D.G.; Stepanov, N.D.; Kuznetsov, A.V.; Kolodiy, I.V.; Tortika, A.S.; Senkov, O.N. Effect of Mn and V on structure and mechanical properties of high-entropy alloys based on CoCrFeNi system. *J. Alloys Compd.* 2014, 591, 11–21.
11. Gludovatz, B.; Hohenwarter, A.; Catoor, D.; Chang, E.H.; George, E.P.; Ritchie, R.O. A fracture-resistant high-entropy alloy for cryogenic applications. *Sci.* 2014, 345, 1153–1158.
12. Tsai, K.Y.; Tsai, M.H.; Yeh, J.W. Sluggish diffusion in Co–Cr–Fe–Mn–Ni high-entropy alloys. *Acta Mater.* 2013, 61, 4887–4897.
13. Owen, L.R.; Pickering, E.J.; Playford, H.Y.; Stone, H.J.; Yucker, M.G.; Jones, N.G. An assessment of the lattice strain in the CrMnFeCoNi high-entropy alloy. *Acta Mater.* 2017, 122, 11–18.
14. Otto, F.; Dlouhy, A.; Somsen, C.; Bei, H.; Eggeler, G.; George, E.P. The influences of temperature and microstructure on the tensile properties of a CoCrFeMnNi high-entropy alloy. *Acta Mater.* 2013, 61, 5743–5755.
15. Singh, S.; Wanderka, N.; Murty, B.S.; Glatzel, U.; Banhart, J. Decomposition in multi-component AlCoCrCuFeNi high-entropy alloy. *Acta Mater.* 2011, 59, 182–190.
16. Kuznetsova, A.V.; Shaysultanov, D.G.; Stepanov, N.D.; Salishchev, G.A.; Senkov, O.N. Tensile properties of an AlCrCuNiFeCo high-entropy alloy in as-cast and wrought conditions. *Mater. Sci. Eng. A* 2012, 533, 107–118.
17. Hemphill, M.A.; Yuan, T.; Wang, G.Y.; Yeh, J.W.; Tsai, C.W.; Chuang, A.; Liaw, P.K. Fatigue behavior of Fatigue behavior of Al<sub>0.5</sub>CoCrCuFeNi high entropy alloys high entropy alloys. *Acta Mater.* 2012, 60, 5723–5734.
18. Pickering, E.J.; Stone, H.J.; Jones, N.G. Fine-scale precipitation in the high-entropy alloy Al<sub>0.5</sub>CrFeCoNiCu. *Mater. Sci. Eng. A* 2015, 645, 65–71.
19. Wang, W.R.; Wang, W.L.; Yeh, J.W. Phases, microstructure and mechanical properties of Al<sub>x</sub>CoCrFeNi high-entropy alloys at elevated temperatures. *J. Alloys Compd.* 2014, 589, 143–152.
20. Chou, H.P.; Chang, Y.S.; Chen, S.K.; Yeh, J.W. Microstructure, thermophysical and electrical properties in Al<sub>x</sub>CoCrFeNi (0 ≤ x ≤ 2) high-entropy alloys. *Mater. Sci. Eng. B* 2009, 163, 184–189.
21. Kao, Y.F.; Chen, T.J.; Chen, S.K.; Yeh, J.W. Microstructure and mechanical property of as-cast, -homogenized, and -deformed Al<sub>x</sub>CoCrFeNi (0 ≤ x ≤ 2) high-entropy alloys. *J. Alloys Compd.* 2009, 488, 57–64.

22. Li, D.; Li, C.; Feng, T.; Zhang, Y.; Sha, G.; Lewandowski, J.J.; Liaw, P.K.; Zhang, Y. High-entropy  $\text{Al}_{0.3}\text{CoCrFeNi}$  alloy fibers with high tensile strength and ductility at ambient and cryogenic temperature. *Acta Mater.* 2017, 123, 285-294.
23. Senkov, O.N.; Woodward, C.; Miracle, D.B. Microstructure and properties of aluminum-containing refractory high-entropy alloys. *JOM.* 2014, 66, 2030-2042.
24. Senkov, O.N.; Senkova, S.V.; Woodward, C. Effect of aluminum on the microstructure and properties of two refractory high-entropy alloys. *Acta Mater.* 2014, 68, 214-228.
25. Qiu, Y.; Hu, Y.J.; Taylor, A.; Styles, M.J.; Marceau, R.K.W.; Ceguerra, A.V. A lightweight single-phase  $\text{AlTiVCr}$  compositionally complex alloy. *Acta Mater.* 2017, 123, 115-124.
26. Senkov, O.N.; Wilks, G.B.; Miracle, D.B.; Chuang, C.P.; Liaw, P.K. Refractory high-entropy alloys. *Intermetallics* 2010, 18, 1758-1765.
27. Guo, S.; Ng, C.; Lu, J.; Liu, C.T. Effect of valence electron concentration on stability of FCC or BCC phase in high entropy alloys. *J. Appl. Phys.* 2011, 109, 645-647.
28. Wang, Q.; Ma, Y.; Jiang, B.B.; Li, X.; Shi, Y.; Dong, C.; Liaw, P.K. A cuboidal B2 nanoprecipitation-enhanced body-centered-cubic alloy  $\text{Al}_{0.7}\text{CoCrFe}_2\text{Ni}$  with prominent tensile properties. *Scripta Mater.* 2016, 120, 85-89.
29. Niu, S.; Kou, H.; Guo, T.; Zhang, Y.; Wang, J.; Li, J. Strengthening of nanoprecipitations in an annealed  $\text{Al}_{0.5}\text{CoCrFeNi}$  high entropy alloy. *Mater. Sci. Eng. A* 2016, 671, 82-86.
30. He, J.Y.; Wang, H.; Huang, H.L.; Xu, X.D.; Chen, M.W.; Wu, Y.; Liu, X.J.; Nieh, T.G. A precipitation-hardened high-entropy alloy with outstanding tensile properties. *Acta Mater.* 2016, 102, 187-196.
31. Ma, K.K.; Wen, H.; Hu, T.; Topping, T.D.; Isheim, D.; Seidman, D.N.; Lavernia, E.J.; Schoenung, J.M. Mechanical behavior and strengthening mechanisms in ultrafine grain precipitation-strengthened aluminum alloy. *Acta Mater.* 2014, 61, 141-155.
32. Reed, R.C. *The superalloys: Fundamentals and Applications*. Cambridge University Press, NY, USA, 2006; pp. 152-157.
33. Wang, X.G.; Liu, J.L.; Jin, T. Sun, X.F. The effects of ruthenium additions on tensile deformation mechanisms of single crystal superalloys at different temperatures. *Mater. Des.* 2014, 63, 286-293.
34. Sato, J.; Omori, T.; Oikawa, K.; Ohnuma, I.; Kainuma, R.; Ishida, K. Cobalt-Base High-Temperature Alloys. *Sci.* 2006, 312, 90-91.
35. Teng, Z.K.; Miller, M.K.; Ghosh, G.; Liu, C.T.; Huang, S.; Russell, K.F.; Fine, M.E.; Liaw, P.K. Characterization of nanoscale NiAl-type precipitates in a ferritic steel by electron microscopy and atom probe tomography. *Scripta Mater.* 2010, 63, 61-64.
36. Jensen, J.K.; Welk, B.A.; Williams, R.E.A.; Sosa, J.M.; Huber, D.E.; Senkov, O.N.; Viswanathan, G.B.; Fraser, H.L. Characterization of the microstructure of the compositionally complex alloy  $\text{Al}_{1.0}\text{Mo}_{0.5}\text{Nb}_{1.0}\text{Ta}_{0.5}\text{Ti}_{1.0}\text{Zr}_{1.0}$ . *Scripta Mater.* 2016, 121, 1-4.
37. Senkov, O.; Isheim, D.; Seidman, D.N.; Pilchak, A.L. Development of a refractory high entropy superalloy. *Entropy* 2016, 18.
38. Mizutani, U. The Hume-Rothery rules for structurally complex alloy phases. *Mrs Bull.* 2012, 37, 2515-2525.
39. Hume-Rothery, W.; Smallman, R.E.; Haworth, C.W. *The structure of metals and alloys*. Metals and Metallurgy Trust, LON, UK, 1969.
40. Egami, T.; Waseda, Y. Atomic size effect on the formability of metallic glasses. *J. Non-Cryst. Solids.* 1984, 64, 113-134.
41. Yang, X.; Zhang, Y. Prediction of high-entropy stabilized solid-solution in multi-component alloys. *Mater. Chem. Phys.* 2012, 132, 233-238.



© 2017 by the authors; licensee *Preprints*, Basel, Switzerland. This article is an open access article distributed under the terms and conditions of the Creative Commons by Attribution (CC-BY) license (<http://creativecommons.org/licenses/by/4.0/>).